Pore-level modeling of drainage: Crossover from invasion percolation fingering to compact flow

M. Ferer
National Energy Technology Laboratory, Morgantown, West Virginia 26507-0880
and Department of Physics, West Virginia University, Morgantown, West Virginia 26506-6315

Grant S. Bromhal
National Energy Technology Laboratory, U.S. DOE, Morgantown, West Virginia 26507-0880

Duane H. Smith
National Energy Technology Laboratory, U.S. DOE, Morgantown, West Virginia 26507-0880
and Department of Physics, West Virginia University, Morgantown, West Virginia 26506-6315
(Received 30 April 2002; revised manuscript received 8 January 2003; published 12 May 2003)

A pore-level model of drainage, which has been quantitatively validated, is used to study the effect of increased injection rate (i.e., increased capillary number) upon the flow, with matched-viscosity fluids. For small enough capillary number, the flows from the model correctly reproduce the flows from the invasion percolation with trapping (IPWT) model. As the capillary number is increased, the early-time flows mimic those of the IPWT-model, but then deviate towards compact flow at a characteristic time that decreases as the capillary number increases. That is, the larger the capillary number, the sooner the flow crosses over from IPWT flows towards compact (linear) flows.

DOI: 10.1103/PhysRevE.67.051601 PACS number(s): 47.55.Mh, 47.53.+n, 47.20.Ma

I. INTRODUCTION

Flow through porous media is a subject of scientific and engineering interest for a number of reasons, e.g., enhanced oil recovery, DNAPL remediation, and geologic CO_2 sequestration. For half a century, flow in porous media has been treated as a compact (i.e., Euclidean) process whereby the interface advances linearly with the total amount of injected fluid. This assumed behavior is predicted by a Darcy's law treatment, which uses saturation-dependent relative permeabilities, such as those of Buckley-Leverett or Koval [1–5]. For the past two decades, it has been appreciated that flow in porous media is fractal in certain well-defined limits [6–15]. In the limit of zero viscosity ratio, $M=\mu_I/\mu_D=0$ (i.e., ratio of the viscosity of the injected fluid to that of the displaced fluid), the flow is known to be modeled by self-similar, diffusion-limited-aggregation (DLA) fractals [6–10,15–20]. Here, the injected fluid has zero viscosity and the displaced fluid has finite viscosity. In the limit of zero-capillary number, where the injection velocity is infinitesimal, $V=0$ (i.e., quasistatic injection), the flow is known to be modeled by self-similar, invasion percolation fractals [21,15]. The definition of the capillary number is

$$N_c=\mu_D V/\sigma\cos\theta, \tag{1}$$

i.e., the ratio of the viscous drag forces (viscosity of the displaced fluid times average fluid velocity, $\mu_D V$) to the capillary forces (proportional to interfacial tension σ times cosine of the contact angle θ). The invasion percolation model has been widely investigated both to determine its fundamental properties and to determine its predictions for practical problems [8,15,21–27].

In a series of papers, we studied unstable (viscosity ratio $M<1$), miscible (zero surface tension) injection using a pore-level model similar to that of Chen and Wilkinson [18], Lenormand [6], and Blunt and King [7]. That is, we performed pore-level modeling of the injection of a less viscous fluid into a model porous medium saturated with a more viscous fluid, with viscosity ratio $M=\mu_I/\mu_D<1$, and zero surface tension. We found that initially the fluid injection was described by DLA fractals; but as the fluid advanced, the injection became compact on a time scale related to the inverse of the viscosity ratio, $1/M$. Hence, the smaller the viscosity ratio, the longer it took for the flow behavior to "cross over" from fractal to compact behavior, so that the only flows that remained fractal were those in the zero viscosity-ratio limit [11–14,28]. This crossover was observed in both two- and three-dimensional flows [11,14]; the crossover affected both the saturation of injected fluid and the interfacial width [12,13]. The behavior of this crossover enabled us to characterize the dependencies of saturation and fractional flow upon the viscosity ratio, in the long-time, compact limit (Buckley-Leverett flow) to which the assumptions of standard Darcy's law flow apply.

Recently, we have modified our earlier code to include the effect of capillary forces to study drainage, where a nonwetting fluid displaces a wetting fluid [29]. In this paper, we focus on the role of capillary forces, which needs to be understood before we undertake the more complicated study of the simultaneous effect of both viscous and capillary forces. Given this focus, we fixed the viscosity ratio at the value unity (viscosity matching) so that the two fluids have identical behavior except for the role of capillary forces. At sufficiently low capillary numbers, we have demonstrated that our model correctly reproduces the zero-capillary number results from the invasion percolation with trapping (IPWT) model [29]. Having validated our model in the limit of small capillary number, where the flow exhibits fractal fingering, we study the effect of increased capillary number on the flow.

Section II briefly discusses salient features of our pore-level model of immiscible drainage; a more detailed description is presented in the Appendix. Sections III and IV present results for a variety of capillary numbers, which show that initially the flows are fractal, mimicking those of the IPWT model but that these flows become compact (linear or stable) after a characteristic time varying inversely with the capillary number. Section III presents results for the first moment of the injected fluid, which tracks the average position of the injected fluid as it invades the model porous medium for several system sizes. Initially, these results for the time dependence of the average position of the injected fluid are identical to results for the average position of the injected fluid from the IPWT model for the same model porous medium; however, at a characteristic time, the motion of the injected fluid deviates from the fractal IPWT model behavior and approaches a linear (constant speed) time-dependent advance of the fluid. This characteristic time is observed to decrease with increasing capillary number. Section IV presents results for the growth of correlations both parallel and perpendicular to the flow. Consistent with the behavior of the average position of the injected fluid, the correlations initially mimic the IPWT model behavior but then break away at a characteristic time approaching the behavior expected from linear flow. These results, showing crossover from the IPWT model flow to compact flow in the average position of the injected fluid, are qualitatively similar to experimental results for the width of the interface [30]. However, to our knowledge, this is the first quantitative observation and characterization of the crossover from demonstrably IPWT model flow at early times towards compact flow at later times.

II. FEATURES OF THE PORE-LEVEL MODEL

Our model is a generic pore-level model of the type that has been widely used for the past two decades [6–18,11–14,16–18,21,23,24,31–36]. Although our model has many features in common with these other pore-level models in the literature, we choose to describe the model in some detail in the Appendix so that the reader can understand how our model compares to the others.

Salient features of our pore-level model include the following.

(i) Our model is intended to incorporate, as realistically as possible, both the capillary pressure that tends to block the invasion of narrow throats and the viscous pressure drop in a flowing fluid.

(ii) The diamond lattice structure assures that all throats are geometrically equivalent with regards to the average flow, in that the throats are not either parallel or perpendicular to the average flow as they would be for a square lattice array.

(iii) All elements of the porous medium (pore throats and pore bodies) have volumes that can be occupied by either fluid.

(iv) We have tried to make the flow rules as nonrestrictive as possible in that (a) locally, back flow as well as forward flow are allowed, as ordained by the local pressure differences, and (b) complications, such as overfilled pore bodies or plugs of fluid trapped in the pore throats, are treated as physically as possible [29].

(v) Most importantly, these flow rules accurately account for all of the nonwetting fluid injected into the porous medium, from initiation through breakthrough over thousands of time steps. For the smallest capillary number, there is a 0.25% difference between the (a) total volume of nonwetting fluid injected into the medium and (b) the total volume of nonwetting fluid occupying the medium as determined by the flow rules. For the largest capillary number, this difference is less than 0.01%.

(vii) Our model has been quantitatively validated in the very different limits of zero-capillary number (agreement with the IPWT model) and zero viscosity ratio (agreement with DLA) [29].

III. RESULTS—CROSSOVER IN THE AVERAGE POSITION OF THE INJECTED FLUID, $\langle x(t)\rangle$

In this section, we study the flow as it deviates from the IPWT model as capillary number increases. Figure 1 compares the near-breakthrough flow patterns for the IPWT model [Fig. 1 (upper left)] with the near-breakthrough patterns for the model with increasing capillary number. For the smallest capillary number shown, $N_c = 2.7\times 10^{-5}$, one sees some additions to the IPWT model pattern, especially in the left-hand third of the figure. As the capillary number is increased, the patterns deviate more and more strongly from the IPWT model.

Because of the engineering interest in maximizing the amount of injected fluid (enhanced oil recovery and carbon dioxide sequestration), it is important to understand how the injected fluid occupies the medium. For this reason, our study has investigated the average position, $\langle x\rangle$, of the injected fluid as a function of the total amount of injected fluid. Since we found, as will be seen, that the IPWT model represented the baseline behavior, it is useful to first study the time dependence of $\langle x(t)\rangle$ for the IPWT model [29]. All distances are in units of the distance between rows of our diamond lattice (Fig. 17), which we have chosen to be unity. All volumes are in units of the volume of a pore body, which we have chosen to be unity.

Our investigation determines the average position $\langle x\rangle$ of the injected fluid as a function of the injected volume V or mass m or time. Since our program maintains a constant volume flow q to within a fraction of a percent, the volume is directly proportional to the time, $V = q\ t$, as is the mass of our incompressible fluids. An additional advantage of determining the time dependence of $\langle x(t)\rangle$ is its simple relationship to fractal dimension for fractal flows like those from the IPWT model. Since the mass of a fractal, m, is related to the linear dimension $\langle x\rangle$, $t \propto m = A\langle x\rangle^{D_f - 1}$, then $\langle x(t)\rangle$ is given by

$$\langle x(t)\rangle = Bt^{1/(D_f-1)} = Bt^{1+\varepsilon}, \tag{2}$$

which defines the exponent ε.

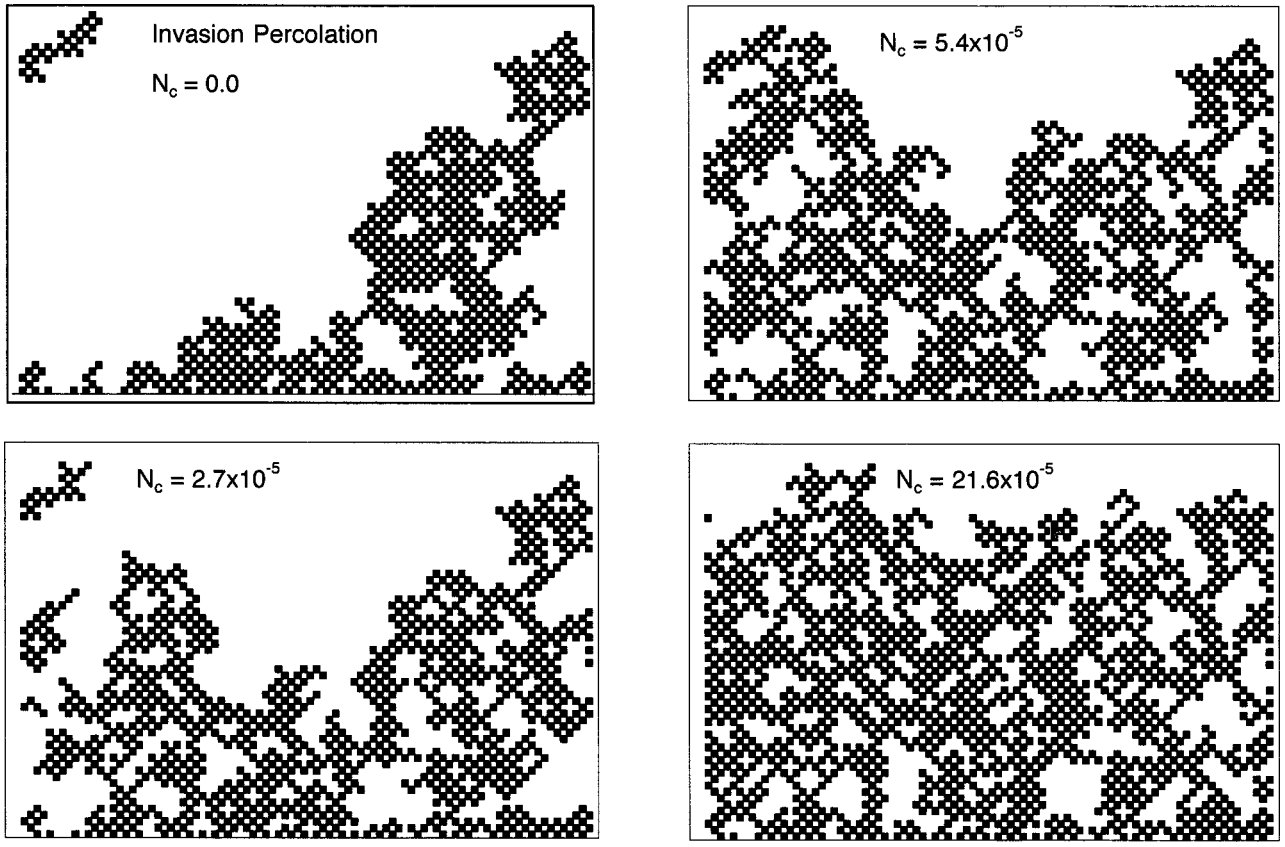

FIG. 1. Comparison of the near-breakthrough IPWT model pattern (upper left) with the near-breakthrough patterns for three capillary numbers ($N_c = 2.7\times10^{-5}$, 5.4×10^{-5}, and 21.6×10^{-5}) using the same realization of a 60×45 model porous medium. The periodic boundary conditions cause the finger growing at the upper right of the IPWT model pattern to extend into the upper left-hand side of this pattern.

A. Results—Limit of the IPWT model

Figure 2 shows data from a variety of IPWT simulations from systems with the size of our flow-model simulations (30×90 up to 30×270 with a few thousand pore bodies) to much larger systems (400×2500 with 10^6 pore bodies). Our definition of "time," $t=(m/w)+0.91$, has the following advantages.

(i) We use the mass m (equivalently the volume, both proportional to the physical time), which will enable us to compare the fractal character from computer experiments with different flow velocities and capillary numbers.

(ii) The time therefore, has the same dimensions as volume, i.e., the unit volume of a pore body.

(iii) Given our uniform injection along the width of the model, we divide the mass by the number of pore bodies along the width w so that the time is unaffected by the width of different size models even though the mass would be proportional to the width.

(iv) The additive constant of 0.91 makes the power law in Eq. (2) applicable over the greatest range (to the smallest times) and arises from the discrete vs, continuous arguments of our earlier miscible flow work [37].

(v) the exponent $1+\varepsilon=1.13$ represents the best fit to this data biasing the data from the large systems more heavily than the data from the small systems.

This value of the exponent $1+\varepsilon=1.13$ is consistent with the fractal dimension $D_f=1+1/(1+\varepsilon)=1.89$, from percolation theory [39]. This value of fractal dimension is somewhat larger than that found in other studies of the IPWT model, $D_f=1.82$ [9,10,15]. However, given the noise in our data, the different lattice structure and the different methods for determining fractal dimension, differences of 4% may not be surprising. These data are sufficiently noisy that they demonstrate only a slight preference for $D_f=1.89$ over the value $D_f=1.82$, which resulted from box counting on larger systems [39,15].

We have focused on "short, wide" systems because experience has shown that flows in long narrow systems (even in square systems) coarsen from many growing fractal fingers to one growing finger. This causes significant deviations from fractal power laws. Also, the wider the system, the less important size effects should be.

B. Results from the flow model with finite capillary number

Most of the results from the flow model are from systems either 30×90 or 30×135 pore bodies. Because invasion percolation is such a noisy process, it proved difficult to study the change from invasion percolation to more pistonlike flow. To show the effect of the noise and how the change away from the IPWT model occurs, Figs. 3(a)–3(d) compare

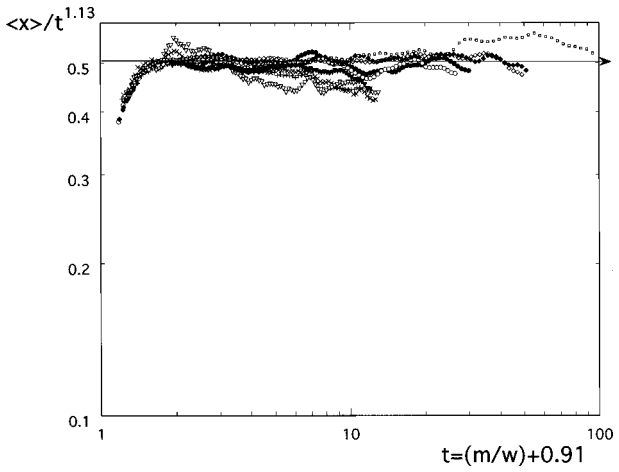

FIG. 2. The fractal scaling of $\langle x(t)\rangle$ from the IPWT model on a variety of systems sizes averaging over a variety of numbers of realizations (samples) [38]. Specifically this figure shows the data from systems of size 400×2500 from averaging over nine realizations (□), systems of size 180×1080 [from averaging over 30 realizations (◇) and over five realizations (◆)], systems of size 90×540 [from averaging over 20 realizations (○) and over only five of the realizations (●)], systems of size 30×135 from averaging over 20 realizations (▼), systems of size 30×90 [from averaging over 20 realizations (+), over seven selected realizations (×), and over the five realizations used for the flow model (▽)]. All distances are in terms of the unit distance between rows of the diamond lattice; all times and volumes are in terms of the unit volume of each pore body.

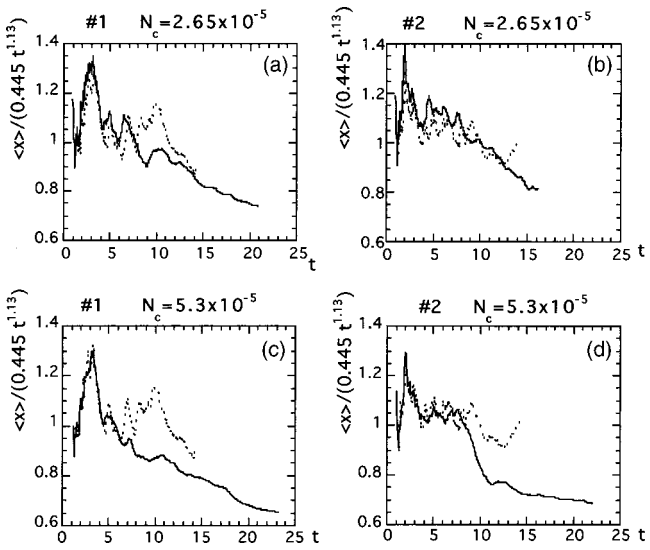

FIG. 3. (a)–(d) Comparisons of flow-model results (solid lines) for two capillary numbers ($N_c=2.65\times10^{-5}$ in the top figures and $N_c=5.3\times10^{-5}$ in the bottom figures) with results from the IPWT model (dashed lines) for the typical realizations number 1 (left-hand figures) and number 2 (right-hand figures) of the five total realizations. Note that the dashed-line curves (the IPWT model) are the same in both figures for realization number 1 (also in both figures for realization number 2). All distances are in terms of the unit distance between rows of the diamond lattice; all times and volumes are in terms of the unit volume of each pore body.

results for invasion percolation (dashed line) with the corresponding results from our model (solid line) for two capillary numbers for the quantity $\langle x\rangle/(0.445t^{1.13})$. The results from the model begin by following the invasion percolation results quite closely but then deviate at a later time, which decreases as the capillary number increases.

To best characterize the deviations from the IPWT model results for each of the five realizations, we determined the ratio $x_{N_c}(t)/x_{\mathrm{IP}}(t)$ until there were significant, sustained deviations from unity; from that point on we used the ratio $x_{N_c}(t)/x_{\mathrm{IP,ave}}(t)$, where $x_{\mathrm{IP,ave}}(t)=0.445t^{1.13}$. These determinations of the ratios were then averaged over the five realizations for each capillary number. These results are presented in Fig. 4 for the systems that are 30×90 and in Fig. 5 for the systems that are 30×135. From these figures, it is clear that initially the flows mimic the IPWT model but then deviate at a later, characteristic time; it is also clear that the larger-capillary-number flows begin to deviate at earlier times.

To estimate the dependence of the characteristic time upon capillary number, we have attempted to collapse all of the data onto one curve (see Figs. 6–8). The form of the characteristic time which most effectively accomplishes this collapse is

$$\tau(N_c)\approx0.02\{\ln(1/N_c)\}^{2.5} \tag{3}$$

where our crude estimate of the uncertainty in the exponent is 2.5 ± 0.5, in that 2.0 is too weak a dependence and 3.0 is too strong a dependence. Clearly, this form for the characteristic time provides a credible collapse of the data so that

$$\langle x(t)\rangle=0.445t^{1.13}F(t/\tau), \tag{4}$$

To ascertain the significance of size effects, we have combined the data from Figs. 6 and 7 in Fig. 8. It is tempting to

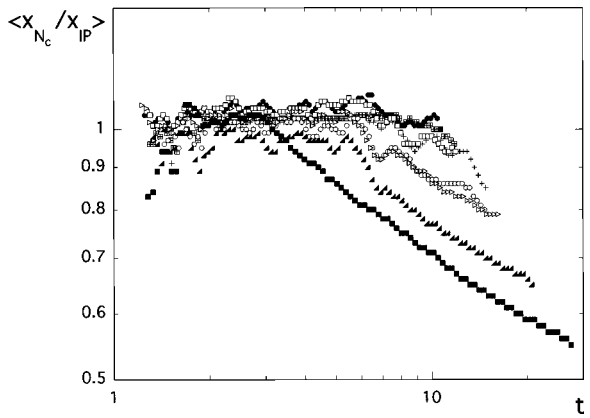

FIG. 4. Data from averaging $x_{N_c}(t)/x_{\mathrm{IP}}(t)$ over five realizations for the 30×90 systems for a variety of capillary numbers $N_c=5.3\times10^{-6}$ (⊞), $N_c=8.8\times10^{-6}$ (●), $N_c=1.33\times10^{-5}$ (+), $N_c=2.65\times10^{-5}$ (□), $N_c=5.3\times10^{-5}$ (○), $N_c=1.06\times10^{-4}$ (▷), $N_c=2.12\times10^{-4}$ (◢), $N_c=8.8\times10^{-4}$ (■). Note: at small t, the value is $\approx1.00\pm0.05$, so that the noise is reduced from the case in Fig. 3 where the values are $\approx1.0\pm0.3$. Figure 2 shows that simply averaging over several realizations does not significantly reduce the noise, especially for these small, near-IPWT model systems.

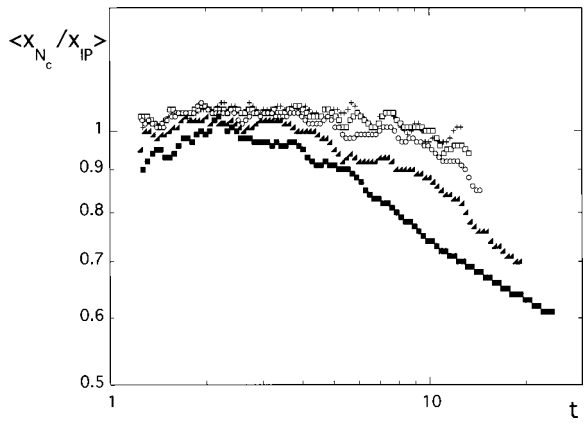

FIG. 5. Data from averaging $x_{N_c}(t)/x_{\mathrm{IP}}(t)$ over five realizations for the 30×135 systems. $N_c=1.33\times10^{-5}$ (+), $N_c=2.65\times10^{-5}$ (□), $N_c=5.3\times10^{-5}$ (○), $N_c=2.12\times10^{-4}$ (◢), $N_c=8.8\times10^{-4}$ (■).

assume that Fig. 8 shows a size dependence in the data, since the crossover for the wider systems occurs slightly later than that for the 30×90 systems. However, further investigation shows that this apparent size dependence is random, likely related to the noise in these small, near-IPWT model systems. Demonstrating the lack of a systematic size dependence, Fig. 9 shows the same plot for several systems of different width with the same capillary number. The crossover does not occur at exactly the same characteristic time for all systems; but the variations appear random rather than systematic, and these variations are of a size that is consistent with other noise observed in these small, near-IPWT model systems. This also shows that edge effects do not significantly affect our results.

The evidence presented shows that initial flows are the IPWT model fractals but that the flows deviate from this fractal behavior at a characteristic time that decreases as one moves away from the IPWT model limit (i.e., as the capillary number increases). We have estimated the dependence of the characteristic crossover time in Eq. (3) and in Figs. 6–8. It is

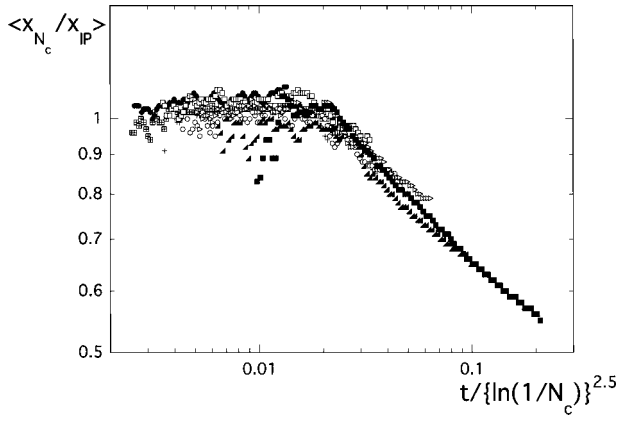

FIG. 6. The collapse of the data from Fig. 4 using the characteristic time in Eq. (3) for capillary numbers [$N_c=5.3\times10^{-6}$ (⊞), $N_c=8.8\times10^{-6}$ (●), $N_c=1.33\times10^{-5}$ (+), $N_c=2.65\times10^{-5}$ (□), $N_c=5.3\times10^{-5}$ (○), $N_c=1.06\times10^{-4}$ (▷), $N_c=2.12\times10^{-4}$ (▶), $N_c=8.8\times10^{-4}$].

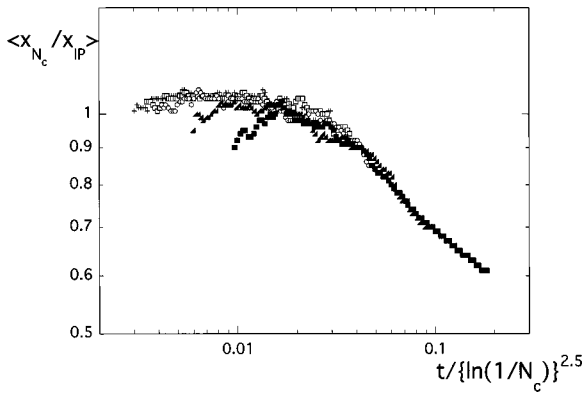

FIG. 7. The collapse of the data from Fig. 5 using the characteristic time in Eq. (3) for capillary numbers [$N_c=1.33\times10^{-5}$ (+), $N_c=2.65\times10^{-5}$ (□), $N_c=5.3\times10^{-5}$ (○), $N_c=2.12\times10^{-4}$ (◢), $N_c=8.8\times10^{-4}$ (■)].

natural to assume that the flows are becoming linear in that the interface (or average position of the injected fluid) advances linearly with time. However, Fig. 10 shows that, at breakthrough, our flows in these small systems have not yet achieved linearity. This figure also shows that the crossover does not occur at one point but over a temporal region of finite width.

In Fig. 10, we normalized the ratio $\langle x_{N_c}/x_{\mathrm{IP}}\rangle$ used in the previous figures by the appropriate time factor so that linear (stable) flow at long times would be a horizontal line (i.e., with zero slope) on the graph. Note that the small-capillary-number fractal regime is increasing with a slope 0.13; however, the large-capillary-number regime has not reached constancy at breakthrough (the latest times shown). The negative slope of the late-time, large-capillary-number plots shows that the flow is occupying the small-x regimes of the porous medium; obviously, this negative slope cannot be maintained indefinitely because eventually the whole porous medium would be filled and the interface would have to advance linearly with the amount of fluid injected. Since our simulations have not achieved linear flow at the latest time accessible to these simulated flows, we will call these intermediate or prelinear-flow times.

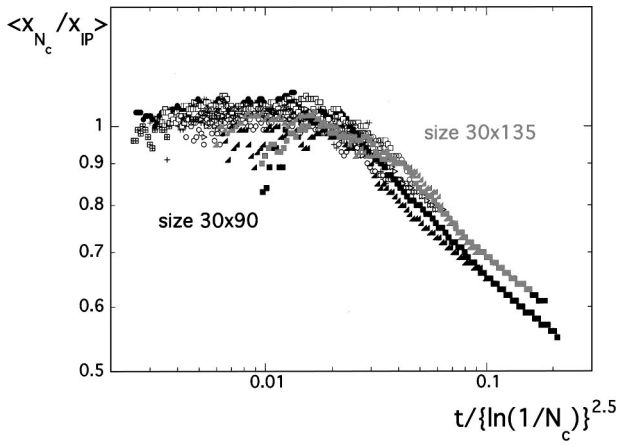

FIG. 8. The data from Figs. 6 and 7 are combined.

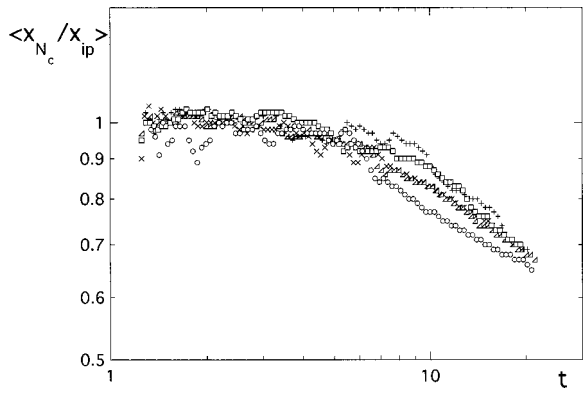

FIG. 9. $\langle x(t)/x_{\mathrm{IP}}\rangle$ vs t for a single capillary number but a variety of widths [sizes 30×90 (○), 30×135 (□), 30×180 (+), 30×225 (△), and 30×270 ×)]. This indicates that the apparent size dependence in Fig. 8 is random.

Although the large-time flows for our small systems have not achieved the linear-flow regime, it is clear that they are tending towards that behavior. Furthermore, the negative slopes in the crossover regime in Fig. 10 cannot be sustained and only represent a temporary filling-in of the small-x regions of the porous medium. Therefore, we have clear evidence for the crossover or transition from early-time IPWT model fractal flow to late-stage linear flow beginning at a characteristic time that varies inversely with the capillary number.

IV. TIME-DEPENDENT CORRELATIONS

The space-time correlations studied in this section are the contributions from all pairs of invaded pore bodies spatially separated by Δx in the average flow direction and by Δy perpendicular to the average flow direction and by Δt in time. That is, the first pore body in the pair located at (x, y) was occupied at time t, while the second pore body at $(x+\Delta x, y+\Delta y)$ was occupied at time $t+\Delta t$. These pairs are averaged over all x and y. Therefore, the correlation function is given by

$$C(\Delta x,\Delta y,t+\Delta t)=\langle n(x+\Delta x,y+\Delta y,t+\Delta t)n(x,y,t)\rangle, \tag{5}$$

where $n(x,y,t)=1$ if the pore body at (x, y) was invaded at time t, and zero otherwise. To study changes in the character of the flow as the fluid advances (i.e., as a function of time t), it is essential to maintain the t dependence, unlike the IPWT model correlations studied in Refs. [40–42] where one averages over this time dependence. In watching the time-dependent simulation of the invasion, the role of avalanches in the IPWT model is clear. During one avalanche, the fluid advance occurs in the localized region of that avalanche; then, the fluid advance occurs in the region of the next avalanche (spatially separated from the previous one); and so forth. Therefore, for Δt less than the lifetime of an avalanche, the correlation function is short range because the correlated sites are usually within one avalanche. With increased capillary number, this avalanche-to-avalanche structure breaks down. First, one sees two spatially separated avalanches occurring simultaneously, and eventually fluid flow is distributed uniformly over the width of the porous medium. This relaxation (or crossover) from independent avalanches to the flow distributed uniformly over the width manifests itself in the mean square fluctuations of the correlations perpendicular to the flow:

$$\langle(\Delta y-\langle\Delta y\rangle)^2\rangle_t = \sum_{\Delta t<\Delta t_{\max}}\sum_{\Delta x\Delta y}(\Delta y-\langle\Delta y\rangle)^2 C(\Delta x,\Delta y,t,\Delta t). \tag{6}$$

To improve statistics, we have also summed over a short $\Delta t<\Delta t_{\max}$. This value of $\Delta t_{\max}$ was chosen to be small compared to the time scale of the flow and is much less than the lifetime of the larger avalanches ($\Delta t_{\max}$ represents 100 time steps for our 10^6 pore-body systems and 20 time steps for our 2700 pore-body systems). Of course, averaging over a large system, Δy is just as likely to be positive as negative so that $\langle\Delta y\rangle\approx0$. For the IPWT model the perpendicular fluctuations, Eq. (6), are consistent with the avalanche structure, see Fig. 11. For small times, $t=0$, when the avalanches are close to the inlet where they tend to be smaller, one has short-time correlations ($\Delta t<\Delta t_{\max}$) spread over the entire width of the porous medium; as the injected fluid moves further into the porous medium with advancing time, the avalanches become larger [42] and the short-time correlations ($\Delta t<\Delta t_{\max}$) become more localized signaled by a decrease in these perpendicular fluctuations. Of course, if one sums over all values of Δt, these total fluctuations extend over the full width of the porous medium, Fig. 11.

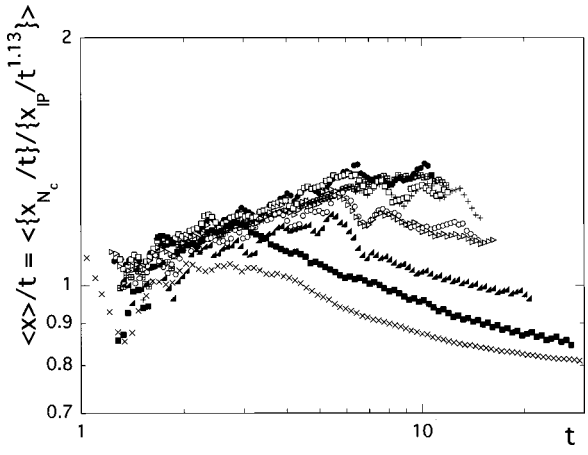

FIG. 10. The average position of the injected fluid divided by time, $\langle x\rangle/t$ for a variety of capillary numbers [$N_c=5.3\times10^{-6}$ (⊞), $N_c=8.8\times10^{-6}$ (●), $N_c=1.33\times10^{-5}$ (+), $N_c=2.65\times10^{-5}$ (□), $N_c=5.3\times10^{-5}$ (○), $N_c=1.06\times10^{-4}$ (▷), $N_c=2.12\times10^{-4}$ (◢), $N_c=8.8\times10^{-4}$ (■), $N_c=3.5\times10^{-3}$ (×)].

Figure 12 shows the perpendicular fluctuations [Eq. (6)] for our 30×90 systems for the IPWT model, as well as for a variety of capillary numbers. For these small systems, the results for the IPWT model exhibit the same decrease seen in Fig. 10, signaling the localization of the short-time correla-

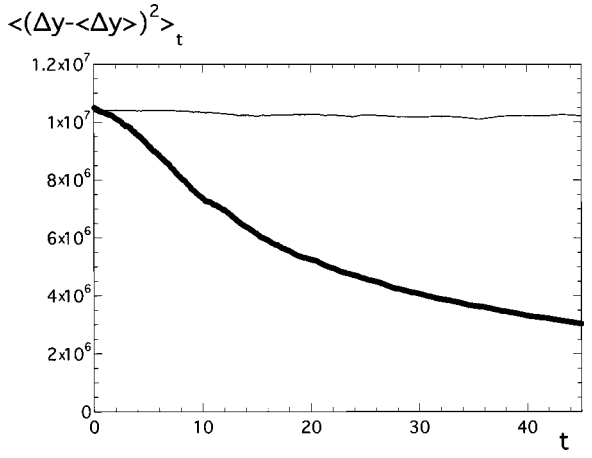

FIG. 11. The perpendicular fluctuations [Eq. (6)] vs time. The heavy solid line shows the short-time [$\Delta t < \Delta t_{\max} = 0.04$ (100 time steps)] perpendicular fluctuations, which decrease with time as the large avalanches begin to dominate, so that short times imply short range correlations within one avalanche. The thinner (nearly horizontal) solid line shows that the long-time (i.e., averaged over all values of Δt) perpendicular fluctuations are spread over the entire porous medium.

tions because of the large, well-defined avalanches for large times. As the capillary number increases, the correlations initially follow the IPWT model behavior and then break away to eventual constant time dependence. When one observes the invasion visually, for small (but nonzero) capillary number, one sees invasion in two separate regions (two simultaneous avalanches). As capillary number continues to increase, the avalanche structure disappears and the invasion occurs randomly over the whole width of the porous medium.

Figure 13 shows the average distance parallel to the flow,

$$\langle \Delta x \rangle_t = \sum_{\mathrm{al_L}} \sum_{\Delta t} \sum_{\Delta x, \Delta y} (\Delta x) C(\Delta x, \Delta y, t, \Delta t), \qquad (7)$$

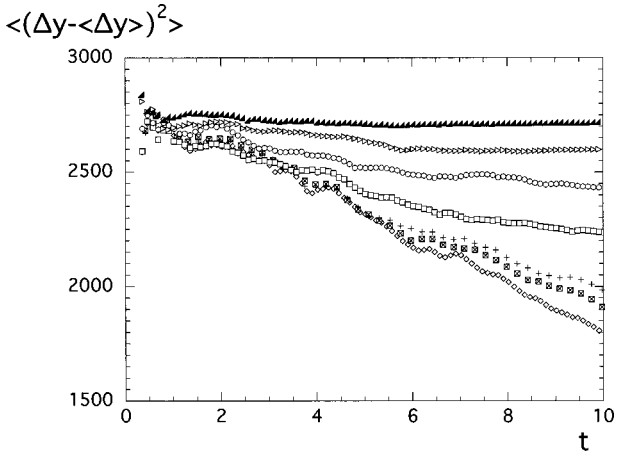

FIG. 12. The short-time [$\Delta t < \Delta t_{\max} = 0.22$ (20 time steps)] perpendicular fluctuations for our 30×90 systems for the IPWT model [$N_c = 0.0$ ($\diamond$)], as well as for a variety of capillary numbers [$N_c = 5.3 \times 10^{-6}$ ($\boxplus$), $N_c = 1.33 \times 10^{-5}$ ($+$), $N_c = 2.65 \times 10^{-5}$ ($\square$), $N_c = 5.3 \times 10^{-5}$ ($\bigcirc$), $N_c = 1.06 \times 10^{-4}$ ($\triangleright$), and $N_c = 2.12 \times 10^{-4}$ ($\blacktriangleleft$)].

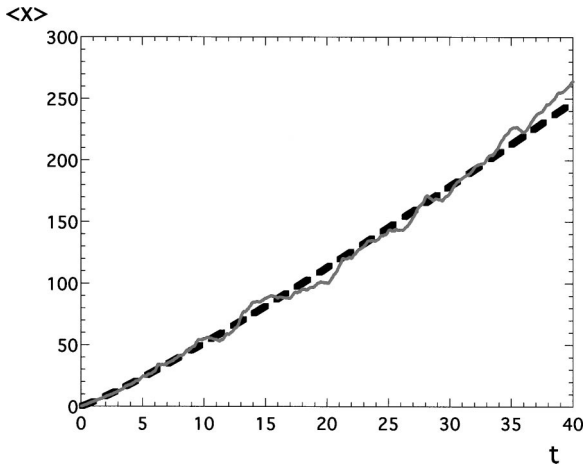

FIG. 13. $\langle \Delta x \rangle_t$ from Eq. (7) (solid gray line), the average separation of correlated pore bodies parallel to the flow, for the large (400×2500) IPWT model systems. The dashed black line shows the best power-law fit to the data ($3.81 t^{1.13}$). Note that the exponent is the same as was used in fitting the average position of the injected fluid.

between correlated pore bodies for the large invasion percolation (the IPWT model) systems. As should be expected, the best power-law fit to these data predicts the same power law as was found for the average position of the injected fluid in Sec. III A. Again the data are sufficiently noisy, so they indicate only a slight preference for the value of fractal dimension $D_f = 1.89$ over $D_f = 1.82$; and again, we emphasize that the main point of our work is not the value of fractal dimension for the IPWT model, but rather the crossover from fractal the IPWT model behavior to linear behavior at a characteristic time that decreases as the capillary number increases, as is clearly shown in Figs. 3–12.

Consistent with the crossover seen in previous figures, Fig. 14 shows $\langle \Delta x \rangle_t$ from Eq. (7) for a variety of capillary numbers. Although these data are much noisier than the data

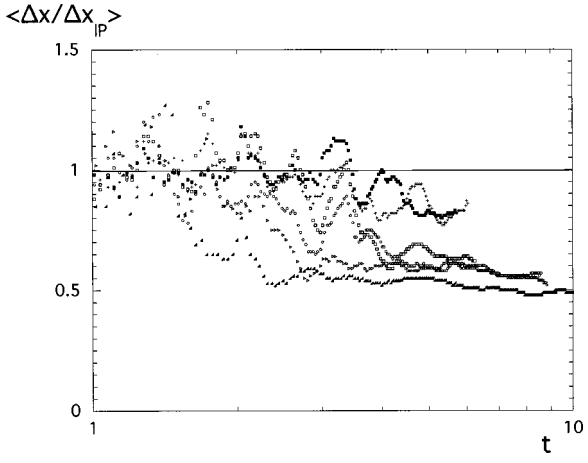

FIG. 14. The mean separation $\langle \Delta x(t) \rangle$ (averaged over all Δt) parallel to the flow for our 30×90 systems for a variety of capillary numbers [$N_c = 5.3 \times 10^{-6}$ ($\boxplus$), $N_c = 1.33 \times 10^{-5}$ ($+$), $N_c = 2.65 \times 10^{-5}$ ($\square$), $N_c = 5.3 \times 10^{-5}$ ($\bigcirc$), $N_c = 1.06 \times 10^{-4}$ ($\triangleright$), and $N_c = 2.12 \times 10^{-4}$ ($\blacktriangleleft$)].

plotted in Figs. 4–10, there is still a clear tendency for the small-capillary-number data to mimic the IPWT model behavior (the horizontal line) while the larger-capillary-number data are consistent with the previously observed crossover from the IPWT model at early times to a behavior consistent with the linear flow (a straight line with a small negative slope $\langle x\rangle/t^{1.13}\propto t^{-0.13}$) at later times.

V. CONCLUSIONS

We have developed a pore-level model of immiscible drainage with the following properties: (i) all pore throats and pore bodies have finite volumes that can be occupied by either fluid, (ii) local flow is dictated only by the local pressure differences, (iii) complications are treated as physically as possible, (iv) the flow rules accurately account for all of the nonwetting fluid injected into the porous medium, (v) the model has been validated (i.e., provides quantitatively correct results) in the limits of zero-capillary number and of zero viscosity ratio [29].

For viscosity matching (viscosity ratio $M=1$) with finite capillary number, the early-time flows mimic those of the invasion percolation with trapping model. At a characteristic time, these flows break away from the IPWT model fractal behavior and approach linear (Buckley-Leverett or ''stable'') flows. The larger the capillary number the sooner this breakaway occurs, i.e., the smaller the characteristic time. This crossover from the IPWT model to compact flow and the associated fractal scaling are qualitatively similar to experimental results for the interfacial width in much larger systems [30]. In this work, we relied on the time dependence of the first moment (average position) of the injected fluid as well as on the time dependence of the parallel and perpendicular correlations because these characteristics of the flow depended upon the time from initial injection to breakthrough, which was necessary to probe the crossover behavior that we found. We found that our systems were too small to provide reliable results from box counting.

The seminal paper of Lenormand, Touboul, and Zarcone [6] demonstrated in what regimes of the viscosity-ratio, capillary-number plane the different flow behaviors (compact flow, viscous fingering, and capillary fingering) dominated. Our results suggest that along the line of unit viscosity ratio large flows only exhibit capillary fingering in the limit of zero-capillary number. That is, solely for zero-capillary number, is there no crossover. For any nonzero capillary number, although the flows will initially exhibit capillary fingering, for large enough flows they will eventually become compact.

The data presented in Sec. III indicate that the characteristic crossover time depends simply upon the capillary number, see Eq. (3). For zero-capillary number, a similar crossover was observed for viscous fingering in porous media, where the flows initially mimicked DLA fractal behavior [43,11–14]. At a characteristic time, these flows break away from the DLA fractal behavior and approach linear (Buckley-Leverett or stable) flows. The larger the viscosity of the injected fluid the sooner this breakaway occurs, i.e., the smaller the characteristic time. In an earlier paper reporting this work, we demonstrated that the power-law behavior

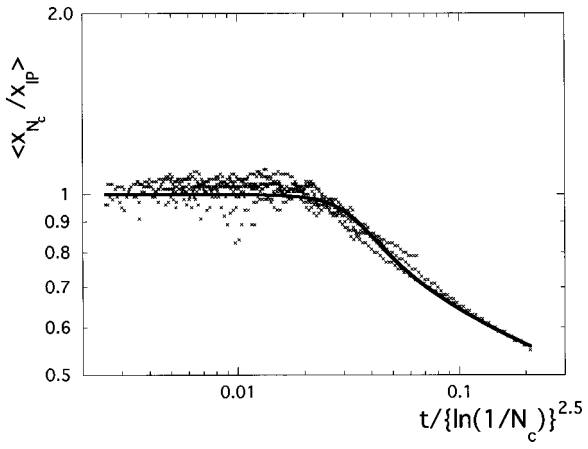

FIG. 15. The heuristic fit (solid line) of the function in Eq. (10) to the data ($\times$) in Fig. 6.

of the first moment and the related power-law behavior of the saturation and fractional flow profiles lead to definite predictions for these profiles in the linear-flow regimes (i.e., post-crossover) [13]. Because of the corresponding relationships between the moment and the profiles for the present case [42] and the corresponding role of the characteristic crossover time [Eq. (3)], one is led to the corresponding behavior for these profiles in the post-crossover regimes ($t\gg\tau$):

$$S(x,t,N_c)=\tau^{-\varepsilon}\sigma(\tau^{-\varepsilon}x/t) \tag{8}$$

and

$$F(S,N_c)=\phi(\tau^{\varepsilon}S), \tag{9}$$

where σ and ϕ are monotonic functions.

These predictions were successfully tested in the previous case [13]. To test these predictions for the present case it is important to have an estimate of when the flows will exhibit linear behavior for different capillary numbers. Towards this end, we have attempted a heuristic fit of the data in Fig. 6, in the hope that such a fit will provide a plausible estimate of when the flows will become linear. As is shown in Fig. 15, this heuristic fit of the data worked credibly for the function

$$\left\langle \frac{x_{N_c}}{x_{\mathrm{IPWT}}} \right\rangle_{\mathrm{fit}} = \{\ln(e+ae^{bu^{0.7}})\}^{-0.13/0.7}, \tag{10}$$

where the best fit gave $a=0.0005\pm0.0002$ and $b=91\pm3$. This function has the correct forms in the small-u and large-u regimes, and it approximates the data reasonably well in the crossover regime. Consequently, we hope that it provides a reasonable estimate of the times at which particular capillary-number flows become linear.

In future work, we plan to check the predictions in Eqs. (8) and (9) guided by the predictions from Fig. 16 that the flows become linear when $t\approx[\ln(1/N_c)]^{2.5}$. We also plan to investigate the changes in the crossover when the viscosities of the two fluids are not equal.

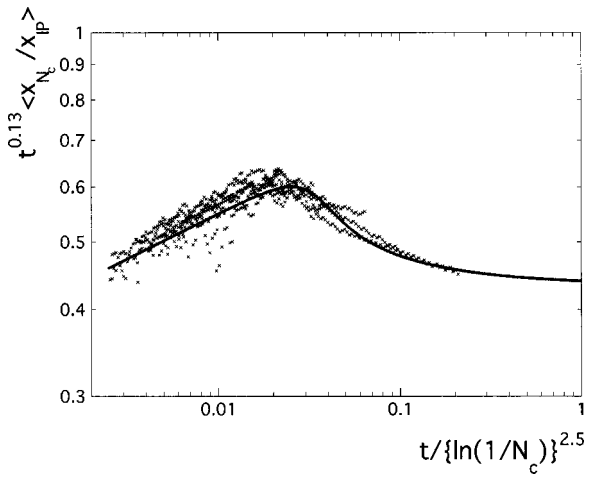

FIG. 16. The behavior of the fitting function (solid line) extended into the regime around $u=1$ where the flow becomes linear.

ACKNOWLEDGMENTS

M.F. and G.B. gratefully acknowledge the support of the U.S. Department of Energy, Office of Fossil Energy. This work was financially supported by National Energy Technology Laboratory.

APPENDIX: DETAILED DESCRIPTION OF THE MODEL

Our model is a generic pore-level model of the type that has been widely used for the past two decades [6–8,11–14,16–18,21,23,24,31–36]. Although our model has many features in common with these other pore-level models in the literature, we choose to describe the model in some detail so that the reader can understand how our model compares to the others. A fully detailed description in the model is included in an earlier paper [29].

Our model is intended to incorporate, as realistically as possible, both the capillary pressure that tends to block the invasion of narrow throats and the viscous pressure drop in a flowing fluid. The two-dimensional porous medium was modeled as a diamond lattice with a length scale ℓ, (Fig. 17). It consists of spherical pore bodies of volume ℓ^3 $[(4\pi/3)r^3=\ell^3]$ at the lattice sites; connecting these pore bodies are cylindrical throats which are of length ℓ, and have a randomly chosen cross-sectional area between 0 and ℓ^2 $(\pi R^2=0\rightarrow\ell^2)$, i.e., there is equal probability for any area between 0 and ℓ^2. Compared to several models reported in the recent literature, we believe that our model should be both more general and more flexible, in part because both the throats and the pore bodies have finite volume in comparison with (i) Refs. [6], [7], [31], where the throats contain zero volume of fluid, and (ii) Refs. [32–35], where the pore bodies have zero volume. Furthermore, in our model, the volumes of both the pore bodies and throats can be set as desired. In this sense the work of Pereira is closer to our model, but the latter work focuses on a model of three-phase flows at constant pressure [36]. Of course all of these models include the essential features of random capillary pressures that block the narrowest throats and a random conductivity that depends on the viscosity ratio.

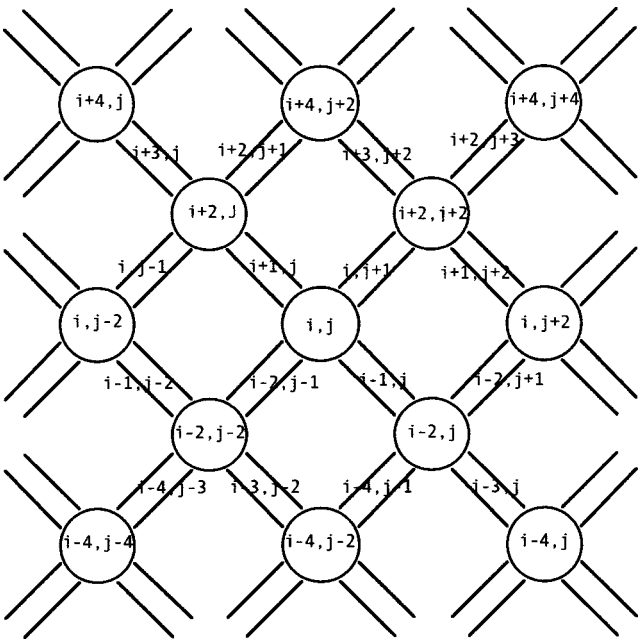

FIG. 17. A portion of the two-dimensional porous medium is shown. The pore bodies, labeled by two even integers, occupy the sites of a diamond lattice. Adjacent pore bodies are connected by pore throats, labeled, as shown, by one even and one odd integer. In this figure, flow is directed upwards, with the inlet being the bottom row of throats, and the outlet being the top. The diamond lattice structure assures that all throats are geometrically equivalent with regards to the average flow, in that the throats are not either parallel or perpendicular to the average flow as they would be for a square lattice array.

In this section, we describe our model briefly; a more complete description was presented in a recent paper [29].

1. Capillary pressure

When the invading fluid first enters one of the pore throats, the radius of curvature R of the meniscus is fixed by contact angle θ and the radius of the pore throat r; $R=r/\cos\theta$. Therefore, the pressure drop across the meniscus is the capillary pressure

$$P_{\mathrm{cap}}(R)=\frac{2\sigma\cos\theta}{r}, \tag{A1}$$

where σ is the surface tension. Thus, the flow velocity is given by the throat conductance times the total pressure drop across the throat, see Fig. 18,

$$q=g_{\mathrm{throat}}(P_{nw}-P_w-P_{\mathrm{cap}}). \tag{A2}$$

In the model, the transmissibility (conductance) of the throat is given by Poiseuille's law,

$$g_{\mathrm{throat}}=g^*\frac{(A^2_{\mathrm{throat}}/\ell^4)}{x+(1-x)M}, \tag{A3}$$

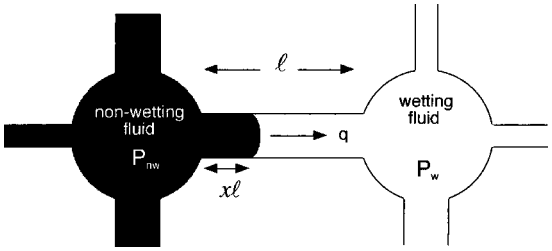

FIG. 18. A sketch showing the advance of the nonwetting fluid within a throat where the pressure drop exceeds the capillary pressure, as given in Eqs. (A1)–(A3).

where A_{throat} is the cross-sectional area of the throat (randomly chosen from a uniform distribution), x is the fraction of the throat of length ℓ which is filled with defending fluid, and M is the ratio of the nonwetting, invading fluid's viscosity to that of the wetting, defending fluid, $M=\mu_I/\mu_D$. The quantity g^* carries all the dimensionality of g_{throat}, $g^*=\ell^3/(8\pi\mu_D)$. Many of our results for the flow velocity are presented in terms of $q^*=q/g^*$, which is independent of the particular value of the viscosity of the wetting fluid. From Eq. (A2), the nonwetting fluid advances if the pressure difference between the pore filled with nonwetting fluid and the pore filled with wetting fluid exceeds the capillary pressure. Otherwise the nonwetting fluid will retreat.

To avoid problems with the abrupt change in capillary pressure at the inlet of a throat, we have adopted the solution used in Refs. [32–35]. Consistent with this work, we assume that the capillary pressure increases from zero at the inlet to a throat of radius r and length ℓ to the value in Eq. (A1) at the center of the throat. This dependence is given by the equation

$$P_{\text{cap}}=\frac{2\sigma\cos\theta}{r}\sin(\pi x), \tag{A4}$$

where x is still the fractional distance along the throat from 0 to 1. Use of Eq. (A4) solves the programming problems caused by the abrupt change in capillary pressure at a throat's inlet because the inlet of a throat will never be blocked since it has a zero-capillary pressure. If blocking occurs, it will occur in the throat where the capillary pressure equals the pressure drop. The earlier work attempted to justify Eq. (A4) physically, by arguing that real throats would have a gradual decrease in cross-sectional area accompanied by a gradual increase in capillary pressure; however, the throat volumes occupied by the fluids were volumes of uniform cylinders [32–35].

2. Finding the pressure field

Volume conservation of the incompressible fluid dictates that the net volume flow q out of any pore body must be zero. Let us consider application of the above rules to the situations in Fig. 19. In Fig. 19, the flow velocities directed out of the (i, j) pore body through the throats are

$$q_{i-2,j-1}=g_{i-2,j-1}(P_{i,j}-P_{i-2,j-2}), \tag{A5a}$$

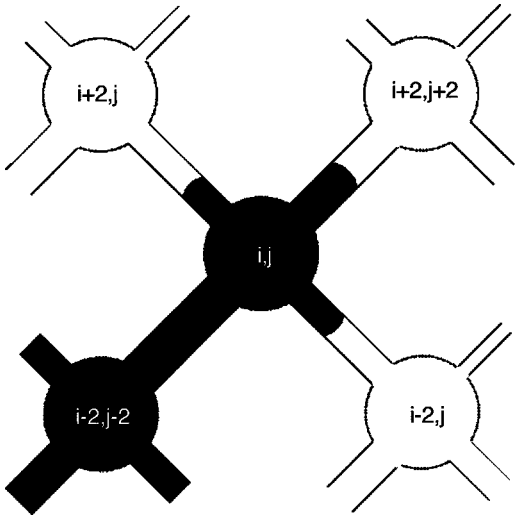

FIG. 19. The fluid occupations near the (i, j) pore giving the flow velocities in Eq. (A5).

$$q_{i,j+1}=g_{i,j+1}(P_{i,j}-P_{i+2,j+2}-P_{\text{cap},i,j+1}),$$

$$q_{i-1,j}=g_{i-1,j}(P_{i,j}-P_{i-2,j}-P_{\text{cap},i-1j}),$$

$$q_{i+1,j}=g_{i+1,j}(P_{i,j}-P_{i+2,j}-P_{\text{cap},i+1,j}).$$

Requiring that the net flow out of the pore body (i, j) be zero leads to the following equation for $P_{i,j}$:

$$\begin{aligned}(g_{i-2,j-1}+g_{i,j+1}+g_{i-1,j}+g_{i+1,j})P_{i,j}&\\ =(g_{i-2,j-1}P_{i-2,j-2}+g_{i,j+1}P_{i+2,j+2}+g_{i-1,j}P_{i-2,j}&\\ +g_{i+1,j}P_{i+2,j})+(g_{i,j+1}P_{\text{cap},i,j+1}+g_{i-1,j}P_{\text{cap},i-1j}&\\ +g_{i+1,j}P_{\text{cap},i+1,j}).&\end{aligned} \tag{A5b}$$

Equation (A5b) is of the general form

$$\left(\sum g\right)P_{i,j}=\left(\sum gP\right)+\left(\sum fgP_{\text{cap}}\right), \tag{A6}$$

where (i) the sums are over the connected throats and pore bodies shown in Fig. 19, (ii) the factor f is zero if there is no meniscus in the throat, (iii) the factor f is $+1$ if the pore body (i, j) is filled with nonwetting fluid and the connecting pore body is filled with wetting fluid, (iv) the factor f is -1 if the pore body (i, j) is filled with wetting fluid and the connecting pore body is filled with nonwetting fluid. Implicit in this discussion is the assumption that the pressure within a pore body is uniform. Assuming otherwise would require doing full fluid dynamics using the Navier-Stokes equations. This is inconsistent with the pore-level model approach and, given finite computer resources, this would severely limit the size of the model porous medium. While Eq. (A4), etc., are idealizations of the real microscopic behavior, the model incorporates the realistic characteristics of a random distribution of conductances and correlated capillary pressures. Significantly, the model has the correct dependencies [Eqs. (A1)–(A3)] upon throat radius for the flow velocity and for the

capillary pressure that must be overcome for the nonwetting fluid to pass through the throat.

Once the location of the interface has been determined, the numerical value of the capillary pressure in each throat is known. The program then iterates Eq. (A6), updating the pressure field until convergence is achieved with a residual less than some small value, that is, until

$$R=\sum\ (P_{\mathrm{new}}-P_{\mathrm{old}})^2<\varepsilon, \tag{A7}$$

where ε is chosen to be small, e.g., $\varepsilon=10^{-3}$ $(\mathrm{dyn/cm^2})^2$. It should be noted that, for the cases being considered, we have used a value of surface tension, such that $2\sigma\cos\theta/\ell=10\,000$ dyn/cm^2. Therefore, the smallest pressure drop that will advance the nonwetting fluid through a throat is 17 700 dyn/cm^2, so that our value of the residual represents a fractional pressure change of less than 10^{-7} in our 2700 pore-body systems. This value of ε was chosen to minimize run time without jeopardizing mass conservation.

3. Flow rules

Once the pressure field has been determined, the interface can be advanced through a time interval Δt. A throat is considered to be on the interface if the pore body at one end contains some wetting fluid (it may be filled with wetting fluid) and if the pore body at the other end is fully invaded by nonwetting fluid (or was fully invaded and is not yet fully reinvaded by wetting fluid due to backflow). We found that the time interval Δt had to be chosen with care. Of course, if the interval is too small, the computer program will be unnecessarily inefficient. However, if the interval is too large, spurious oscillations occur in the fluid flow about the true equilibrium. Having determined the interface and chosen the time step, we have attempted to make the flow rules as unrestrictive as possible.

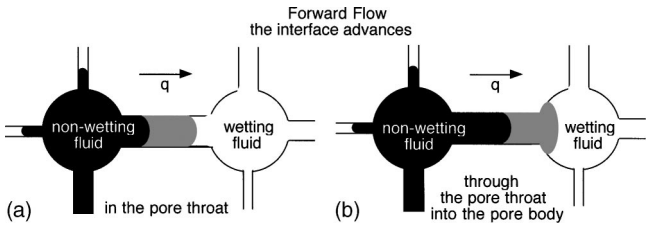

FIG. 20. The flow rules allow the interface to advance (a) within a throat (left figure) as well as (b) through a throat into the adjacent pore body (right figure).

Flow can increase the amount of nonwetting fluid within the pore throat [Fig. 20(a)], or the amount passing through the pore throat into the pore body [Fig. 20(b)]. Similarly, backflow can cause the interface to retreat within the pore throat, or through the pore throat into the pore body. Consistent with Refs. [32–35], the flow rules assume that the throats are cylindrical with cross section A and length ℓ.

In summary, we have attempted to make the flow rules as nonrestrictive and reliable as possible.

[1] R. J. Blackwell, J. R. Rayne, and W. M. Terry, Trans. AIME **216**, 1 (1959).

[2] R. E. Collins, *Flow of Fluids through Porous Materials* (Reinhold, New York, 1961).

[3] J. Bear, *Hydraulics of Ground Water* (McGraw-Hill, New York, 1979).

[4] F. A. L. Dullien, *Porous Media: Fluid Transport and Pore Structure* (Academic, New York, 1979).

[5] H.-K. Rhee, R. Aris, and N. R. Amundson, *First-Order Partial Differential Equations: Vol. I (Theory and Applications of Single Equations)* (Prentice Hall, Englewood Cliffs, NJ, 1986).

[6] R. Lenormand, E. Touboul, and C. Zarcone, J. Fluid Mech. **189**, 165 (1988).

[7] M. Blunt and P. King, Phys. Rev. A **42**, 4780 (1990).

[8] M. Sahimi, *Flow & Transport in Porous Media & Fractured Rock From Classical Models to Modern Approaches* (VCH, Verlagsgesellschaft, Weinheim, 1994).

[9] J. Feder, *Fractals* (Plenum, New York, 1988).

[10] T. Vicsek, *Fractal Growth Phenomena* (World Scientific, Singapore, 1989).

[11] M. Ferer *et al.*, Phys. Rev. A **45**, R6973 (1992).

[12] M. Ferer and D. H. Smith, Phys. Rev. E **49**, 4114 (1994).

[13] M. Ferer *et al.*, AIChE J. **49**, 749 (1995).

[14] M. Ferer, J. Gump, and D. H. Smith, Phys. Rev. E **53**, 2502 (1996).

[15] P. Meakin, *Fractals, Scaling, and Growth Far From Equilibrium* (Cambridge University Press, Cambridge, 1998).

[16] M. Sahimi, H. T. Davis, and L. E. Scriven, Chem. Eng. Commun. **23**, 329 (1983).

[17] M. Sahimi and A. O. Imdakm, J. Phys. A **21**, 3833 (1988).

[18] J.-D. Chen and D. Wilkinson, Phys. Rev. Lett. **55**, 1892 (1985).

[19] J. Nittmann, G. Daccord, and H. E. Stanley, Nature (London) **314**, 141 (1985).

[20] G. Daccord, J. Nittmann, and H. E. Stanley, Phys. Rev. Lett. **56**, 336 (1986).

[21] D. Wilkinson and J. F. Willemsen, J. Phys. A **16**, 3365 (1983).

[22] D. Wilkinson, Phys. Fluids **28**, 1015 (1984).

[23] N. Martys, M. Cieplak, and M. Robbins, Phys. Rev. Lett. **66**, 1058 (1991).

[24] M. O. Robbins *et al.*, Phys. Rev. Lett. **71**, 2074 (1993).

[25] D. Wilkinson, Phys. Rev. A **30**, 520 (1984).

[26] D. Wilkinson, Phys. Rev. A **34**, 1380 (1986).

[27] J. F. Gouyet, M. Rosso, and B. Sapoval, Phys. Rev. B **37**, 1832 (1988).

[28] It should be noted that in this series of earlier papers, the inverse viscosity ratio was used, i.e., $M_{\mathrm{earlier}}=1/M$.

[29] M. Ferer, G. S. Bromhal, and D. H. Smith, Physica A **319**, 11 (2003).

[30] O. I. Frette *et al.*, Phys. Rev. E **55**, 2969 (1997).

[31] S. C. van der Marck, T. Matsuura, and J. Glas, Phys. Rev. E **56**, 5675 (1997).

[32] E. Aker, *A Simulation for Two-Phase Flow in Porous Media* (University of Oslo, Oslo, 1996).

[33] E. Aker *et al.*, Transp. Porous Media **32**, 163 (1998).
[34] E. Aker, K. Jørgen-Måløy, and A. Hansen, Phys. Rev. E **58**, 2217 (1998).
[35] E. Aker, K. Jørgen-Måløy, and A. Hansen, Phys. Rev. E **61**, 2936 (2000).
[36] G. Pereira, Phys. Rev. E **59**, 4229 (1999).
[37] M. Ferer *et al.*, Phys. Rev. E **47**, 2713 (1993).
[38] The only difference between two realizations is the specific choice of the cross-sectional area of the throats. That is, for each realization there is a unique random number seed which is used to start the random choice of the cross-sectional areas of the throats.
[39] D. S. Stauffer, *Introduction to Percolation Theory* (Taylor & Francis, Philadelphia, 1985).
[40] L. Furuberg *et al.*, Phys. Rev. Lett. **61**, 2117 (1988).
[41] S. Roux and E. Guyon, J. Phys. A **22**, 3693 (1989).
[42] M. Ferer, G. S. Bromhal, and D. H. Smith, Physica A **311**, 5 (2002).
[43] M. Ferer *et al.*, Physica A **177**, 273 (1991).